


Article

Construction of S-Scheme 2D/2D Crystalline Carbon Nitride/BiOIO₃ van der Waals Heterojunction for Boosted Photocatalytic Degradation of Antibiotics

Xiangyuan Kong ^{1,*}, Longwen Cao ², Yuxing Shi ², Zhouze Chen ², Weilong Shi ^{2,*}  and Xin Du ^{3,*}¹ School of Physical Science and Engineering, Beijing Jiaotong University, Beijing 100091, China² School of Material Science and Engineering, Jiangsu University of Science and Technology, Zhenjiang 212003, China; czz990707@163.com (Z.C.)³ College of Chemistry, Zhengzhou University, Zhengzhou 450001, China

* Correspondence: 20272038@bjtu.edu.cn (X.K.); shiwl@just.edu.cn (W.S.); dux@zzu.edu.cn (X.D.)

Abstract: Utilization of semiconductor photocatalyst materials to degrade pollutants for addressing environmental pollution problems has become a research focus in recent years. In this work, a 2D/2D S-scheme crystalline carbon nitride (CCN)/BiOIO₃ (BOI) van der Waals heterojunction was successfully constructed for effectively enhancing the degradation efficiency of antibiotic contaminant. The as-synthesized optimal CCN/BOI-3 sample exhibited the highest efficiency of 80% for the photo-degradation of tetracycline (TC, 20 mg/L) after 120 min visible light irradiation, which was significantly higher than that of pure CCN and BOI. The significant improvement in photocatalytic performance is mainly attributed to two aspects: (i) the 2D/2D van der Waals heterojunction can accelerate interface carriers' separation and transfer and afford sufficient active sites; (ii) the S-scheme heterojunction elevated the redox capacity of CCN/BOI, thus providing a driving force for the degradation reaction. The degradation pathways of TC for the CCN/BOI composite were investigated in detail by liquid chromatography-mass spectrometry (LC-MS) analysis. This work provides a design idea for the development of efficient photocatalysts based on the 2D/2D S-scheme van der Waals heterojunctions.

Keywords: S-scheme; 2D/2D; crystalline carbon nitride; BiOIO₃; van der Waals heterojunction



Citation: Kong, X.; Cao, L.; Shi, Y.; Chen, Z.; Shi, W.; Du, X. Construction of S-Scheme 2D/2D Crystalline Carbon Nitride/BiOIO₃ van der Waals Heterojunction for Boosted Photocatalytic Degradation of Antibiotics. *Molecules* **2023**, *28*, 5098. <https://doi.org/10.3390/molecules28135098>

Academic Editors: Barbara Bonelli and Hai-yang Liu

Received: 12 June 2023

Revised: 27 June 2023

Accepted: 27 June 2023

Published: 29 June 2023



Copyright: © 2023 by the authors. Licensee MDPI, Basel, Switzerland. This article is an open access article distributed under the terms and conditions of the Creative Commons Attribution (CC BY) license (<https://creativecommons.org/licenses/by/4.0/>).

1. Introduction

Over the past few decades, antibiotics have been used in a wide variety of fields and have become an essential part of people's lives. However, overuse and mishandling of antibiotics makes it easy for them to accumulate in the environment and pose a health risk to humans and other organisms [1]. There is thereby an urgent need to remove antibiotics from the environment, but it is still a significant challenge. In recent years, researchers have tried to use conventional physical adsorption, biological filtration, chemical treatment, and other methods to eliminate antibiotics [2–5]. Unfortunately, these methods are difficult to apply in practice due to process complexity, the cost of the facilities, and potential secondary contamination [6–8].

Recently, semiconductor photocatalysis has attracted a great deal of attention due to its ability to harness solar energy efficiently and its economic applicability. Among the various photocatalysts, carbon nitride (CN) stands out due to its non-toxicity, stability, excellent optical properties, and suitable electronic structure [9,10]. Nevertheless, some inherent characteristics of CN, such as easy recombination of photo-generated carriers, low specific surface area, and its few active sites, greatly limit the application of CN in the photocatalytic field [11,12]. To overcome the shortcomings of CN, researchers have developed numerous strategies for its use, such as designing morphological structures [13–17], building heterojunctions [18–21], and improving crystallinity [22–24]. Among these modification methods,

it was found that increasing crystallinity to form crystalline CN (CCN) could remove the high-density defects and terminal amino groups in CN, thus effectively inhibiting the recombination of photogenerated electron-hole pairs and enhancing the charge carrier migration rate of CN [25,26]. Furthermore, hybridizing two-dimensional (2D) CN with other semiconductors to construct a 2D/2D van der Waals (VDW) heterojunctions is also a promising strategy for enhancing the photocatalytic activity of CN. Compared to normal heterojunctions, the 2D/2D VDW heterojunctions possess strong interactions and large interface areas due to the unique morphology of materials, which provides channels for the transportation of charge carriers and facilitates carrier transfer rate [27,28]. Moreover, the transfer path of photo-generated electrons in the heterojunction also plays an important role in the effectiveness of the fabricated photocatalyst [29,30]. Notably, step-scheme (S-scheme) heterojunctions raised from Yu's group possesses various unique advantages, which not only promote photo-induced charge separation but also enable the photocatalyst to keep stronger reduction and oxidation capabilities [31–33]. In S-scheme heterojunctions, the e^- and h^+ spatial separations are located on the conduction band (CB) and valence band (VB), respectively. Accordingly, e^- tends to remain at a more negative potential for reduction, while h^+ tends to remain at a more positive potential for oxidation, resulting in a stronger redox ability while effectively inhibiting charge recombination [34–38]. Consequently, the construction of a 2D/2D S-scheme CCN-based VDW heterojunction is necessary for the development and utilization of the enhanced treatment of degraded wastewater with various antibiotics.

Bismuth-based semiconductors have recently become a hot topic in the field of photocatalysts [37]. Bismuth oxiodate (BiOIO_3), a new member of the bismuth-based semiconductor family, exhibits excellent photocatalytic activity due to its favorable physicochemical properties and unique asymmetric sheet structure [39,40]. Furthermore, the two isolated cation pairs (Bi^{3+} and I^{5+}) of BiOIO_3 and the structure exhibiting an Aurivillius-type $(\text{Bi}_2\text{O}_2)^{2+}$ layer with an intercalated $(\text{IO}_3)^-$ anion can play a role in promoting photo-induced carrier migration and separation [41]. It is worth noting that BiOIO_3 with a wide band gap (3.1 eV) is one of the most suitable candidates to meet the energy band alignment to construct heterojunctions with CN [42]. Consequently, inspired by the above considerations, the construction of S-scheme 2D-2D VDW heterojunctions between BiOIO_3 and CCN could create an even more excellent activity.

In this work, an S-scheme 2D/2D CCN/BOI VDW heterojunction photocatalyst was successfully fabricated via a simple hydrothermal method, which exhibited excellent photocatalytic activity in degrading tetracycline antibiotics. Moreover, the as-synthesized materials achieved the best photocatalytic performance by adjusting the ratio of CCN to BOI, which is remarkably higher than that of pure CCN and BOI. Furthermore, the enhanced photocatalytic performance of CCN/BOI composites and the reaction mechanism of S-scheme 2D/2D VDW heterojunctions were investigated and discussed through a series of characterization analyses and theoretical calculations.

2. Results and Discussion

The diagram of the synthesis mechanism of 2D/2D CCN/BOI heterojunction is displayed in Figure 1a. Initially, the CCN nanosheets were synthesized by a one-step rapid polymerization strategy by direct calcination of melamine at 550 °C, without an early heating process, and also without the help of any additives or salt intercalation. Subsequently, during the hydrothermal reaction, the BOI nanosheets were fabricated by controlling the acidity of the solution, while the CCN nanosheets with a large H^+ thermodynamic driving force were successfully coupled to the BOI nanosheets by the VDW driving force to form a 2D/2D CCN/BOI heterojunction. Furthermore, the morphological features and crystal structures of the as-synthesized samples were clearly characterized by transmission electron microscopy (TEM) and high-resolution TEM (HRTEM). As displayed in Figure 1b, the pure CCN exhibits an irregular layered nanosheet structure, while the bare BOI presents a thin nanosheet morphology (Figure 1c). Notably, the scanning electron microscopy (SEM,

Figure S1a) image reveals that the overall morphology of the composite remains as a lamellar structure, and the energy dispersive X-ray spectrum (EDS, Figure S1b) demonstrates the presence of the corresponding C, N, Bi, O, and I elements in the material. Furthermore, the large area and tight contacts at the 2D/2D interface can facilitate the formation of heterojunctions (Figure 1d,e). Remarkably, in the HRTEM image (Figure 1f) of the CCN/BOI-3 composite, it can be observed that the CCN nanosheets are attached to the surface of the BOI nanosheets. Meanwhile, the two different lattice fringes can be noticed in the local magnification of the HRTEM image in Figure 1g, and the 0.289-nm and 0.33-nm lattice fringes belong to the (002) plane of BOI and the (002) plane of CCN, respectively [43,44]. Notably, the observed intimate interface between CCN and BOI implies that the final synthesized CCN/BOI compounds has been obtained by van der Waals heterojunctions. Furthermore, the high-angle ring dark-field (HAADF) and the corresponding elemental mapping images (Figure 1h) display that the elements of C, N, Bi, I, and O are uniformly distributed in the CCN/BOI-3 composite, which indicates that the CCN has been successfully coupled to the BOI.

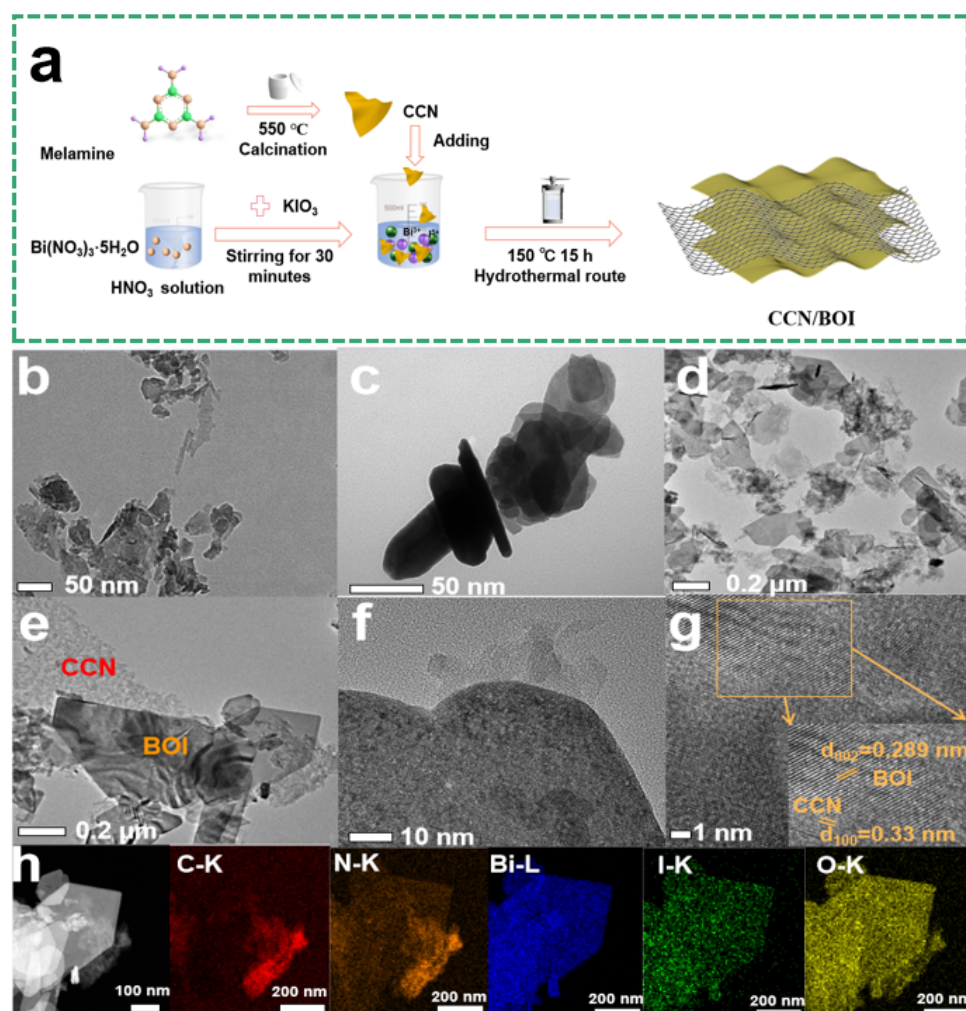


Figure 1. (a) Schematic diagram of the synthetic route over CCN/BOI heterojunction photocatalyst. TEM images of (b) CCN, (c) BOI, (d,e) CCN/BOI-3. (f,g) HRTEM images of CCN/BOI-3. (h) HAADF and elemental mapping images of CCN/BOI-3.

The composition, phases, and crystal structures of pure CCN, BOI, and CCN/BOI composites were determined by X-ray diffraction (XRD), and the results are displayed in Figure 2a. For bare CCN, the two different diffraction peaks located at 13.3° and 27.4° can be attributed to the (100) and (002) crystal planes of CN [45], which correspond

to the in-plane stacking structure of the conjugated aromatic group and the in-plane structural stacking of the tris-triazine unit, respectively [46]. Compared with the BCN, the diffraction peak intensity of the CCN increased significantly, indicating an improved crystallinity (Figure S2). For pure BOI, the characteristic peaks at 27.36° , 31.11° , 31.61° , 32.46° , and 32.96° can be indexed to (121), (002), (200), (040), and (131) crystal planes of the orthorhombic BiOIO_3 (JPCDS No. 26-2019), respectively [47]. Meanwhile, for the profile of the as-synthesized composites CCN/BOI, the diffraction peaks can be indexed to BOI and CCN, which indicates the successful coupling of CCN with BOI. Furthermore, the Fourier transform infrared spectroscopy (FT-IR) spectra of the as-synthesized samples are exhibited in Figure 2b. For pristine CCN, the peak at 808 cm^{-1} corresponds to the characteristic breathing pattern of the s-triazine unit, while the peak in the region around 3000 cm^{-1} is attributed to the stretching vibration of the N-H bond [48]. For pure BOI, the two peaks located at 686 and 767 cm^{-1} are ascribed to stretching vibrations of the I-O bond, and the peak at 515 cm^{-1} is associated with stretching vibrations of the Bi-O bond [49,50]. Furthermore, the broad peak at 3430 cm^{-1} is assigned to a bending vibration of the O-H group, indicating the presence of hydroxyl groups on the surface of BOI [51]. The characteristic peaks belonging to both CCN and BOI are observed in CCN/BOI composites, which indicates that the CCN and BOI are indeed coupled, in agreement with the XRD results. The elemental chemical states, compositions, and interactions between CCN and BOI were characterized by X-ray photoelectron spectroscopy (XPS) measurement. The full XPS survey spectra in Figure 2c confirm that C, N, Bi, O, and I elements all exist in the as-synthesized CCN/BOI-3 composite. As exhibited in Figure 2d, the strong peaks located at 284.63 , 287.85 , and 293.37 eV in CCN are assigned to the C-C single bond with sp^2 hybridization, the sp^2 -hybrid C (N-C=N) coordination in the triazine ring, and π -excitation, respectively [52]. In Figure 2e, the N 1s spectrum of CCN exhibits three peaks at 398.31 , 400.15 , and 404.13 eV , which are ascribed to the sp^2 nitrogen atoms (C-N=C), N-(C)₃ groups, and N-H bonds, respectively [53,54]. The Bi 4f spectrum of BOI consists of two peaks at 159.10 and 164.38 eV , as seen in in Figure 2f, which correspond to Bi 4f_{7/2} and Bi 4f_{5/2}, indicating that Bi exists in the state of Bi^{3+} [40]. In Figure 2g, the O 1s spectrum of BOI can be deconvoluted into two peaks at 530.14 and 531.48 eV , corresponding to the lattice oxygen I-O [7]. Furthermore, the I 3d spectrum of BOI exhibited two peaks at 623.61 and 635.11 eV (Figure 2h), belonging to I 3d_{5/2} and I 3d_{3/2}, indicating that element I is present in the +5 valence state [55]. Notably, the shift of binding energy clearly demonstrates the transfer of photo-induced electrons from BOI to CCN, indicating the strong coupling between CCN and BOI with the formation of heterojunctions in the BOI/CCN composite.

The optical absorption properties of the as-synthesized samples were analyzed by UV-vis diffuse-reflectance measurement, and the results are exhibited in Figure 3a. It can be observed that the absorption peaks of pure CCN and BOI are located at 460 and 405 nm , respectively, which are mainly attributed to the intrinsic band gaps of CCN and BOI [56]. With the gradual increase of the introduced CCN content, the absorption edge of CCN/BOI-x composites appear to red-shift and the light absorption intensities have been significantly enhanced (digital photographs are given in Figure S3), which are mainly ascribed to the successful combination of CCN and BOI to promote the transfer of photogenerated carriers and substantially improve the light utilization efficiency. Moreover, the band gap energies of pure CCN and BOI can be calculated by the following equations: $\alpha hv = A(hv - E_g)^{n/2}$, where α , hv , A , E_g , and n are the absorption coefficient, photon energy, constant, band gap energy, and constant determined by the type of optical transition of the semiconductor material, respectively [57]. Based on the equation, the calculated band gaps for pure CCN and BOI are 2.42 and 3.13 eV , as seen in Figure 3b, which is consistent with previous reports [58,59]. Furthermore, Mott-Schottky (M-S) analysis was applied to measure the actual band edge positions of pure CCN and BOI (Figure 3c). The flat band potentials of CCN and BOI were estimated by extrapolating to $C^{-2} = 0$ at 800 , 1000 , and 1200 Hz , which are -0.51 and -0.40 V , respectively (vs. Ag/AgCl). Furthermore, the conduction band (CB) potential of n-type semiconductors is approximately equivalent to the flat-band

potential [60]. Consequently, the CB potentials of CCN and BOI are approximately -0.51 and -0.40 eV, respectively, while the VB positions are 1.91 and 2.73 eV ($E_{CB} = E_{VB} - E_g$), respectively. The corresponding band structures of CCN and BOI are exhibited in Figure 3d.

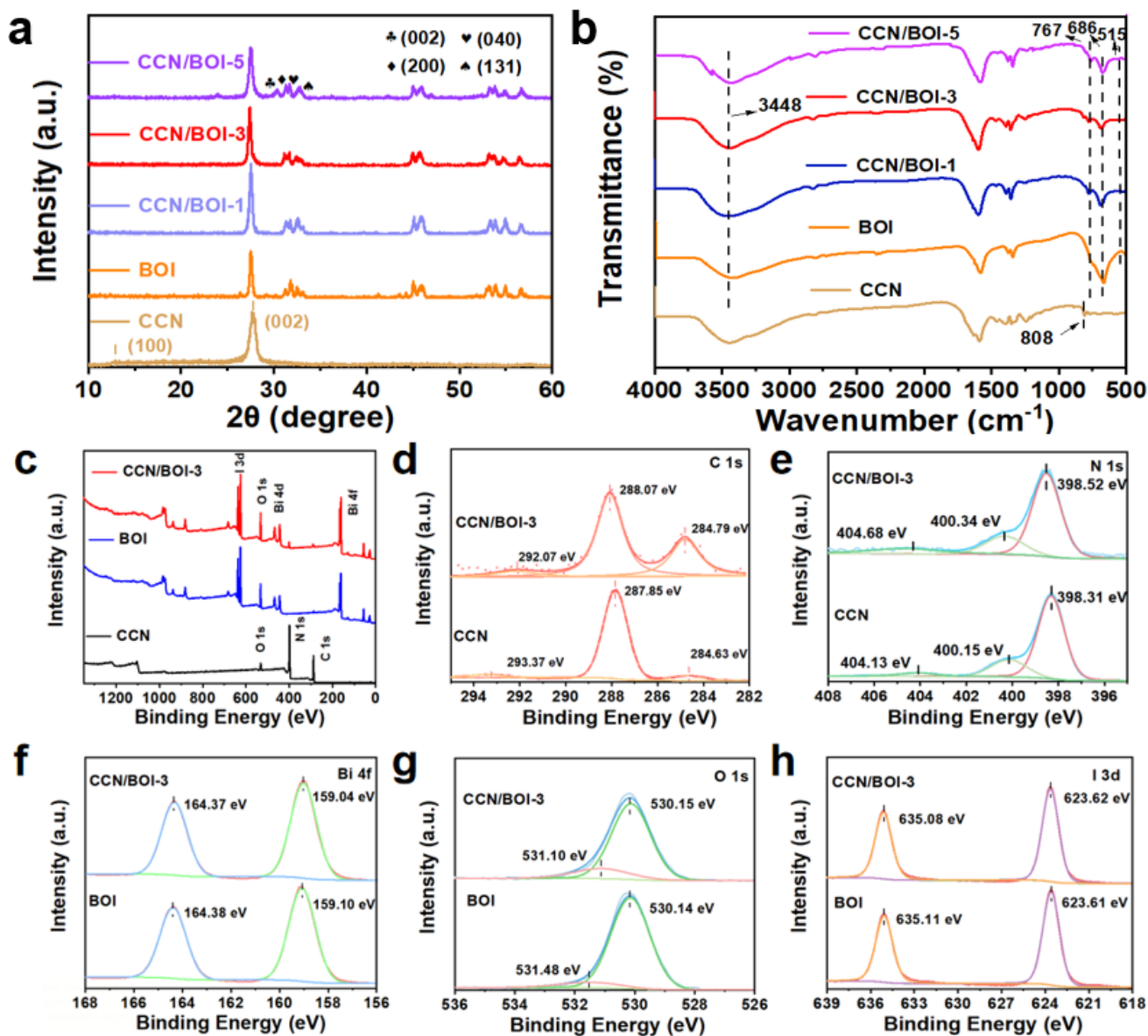


Figure 2. (a) XRD patterns and (b) FT-IR spectra of the as-synthesized CCN, BOI, and CCN/BOI heterojunctions. (c) XPS survey and high-resolution spectra of CCN, BOI, and CCN/BOI-3: (d) C 1s; (e) N 1s; (f) Bi 4f; (g) O 1s; (h) I 3d.

The photocatalytic performance of the as-synthesized photocatalysts was evaluated by the degradation of tetracycline (TC) under visible light conditions. As displayed in Figure 4a, the TC was hardly decomposed under dark conditions, while the photocatalysts clearly degraded the TC under visible light irradiation (Figure 4b). It was observed that the photocatalytic activity of the pure 2D layered CCN and 2D BOI nanosheets was poor, with a degradation rate of 36% and 41%, respectively, which were attributed to the poor visible light absorption of both materials and the rapid recombination of photogenerated charge carriers. Significantly, the CCN/BOI-3 composite exhibited the best photocatalytic activity with the degradation rate of 79.8%, which is superior to that of previously reported CN- or

BOI-based reaction systems (Table S1). Moreover, the time course variation curve of TC can be further described by the kinetic equation (Equation (1))

$$\ln(C_0/C) = kt \tag{1}$$

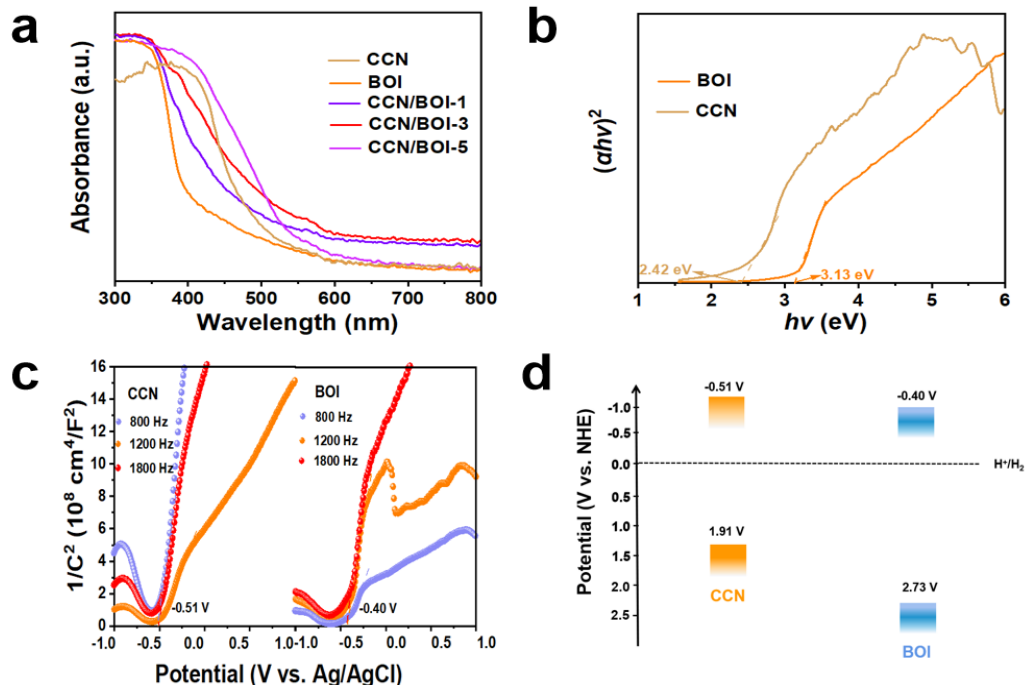


Figure 3. (a) Diffuse reflectance spectra of as-prepared samples. (b) Kubelka–Munk plots of CCN and BOI. (c) M–S plots and (d) the corresponding band structures of CCN and BOI.

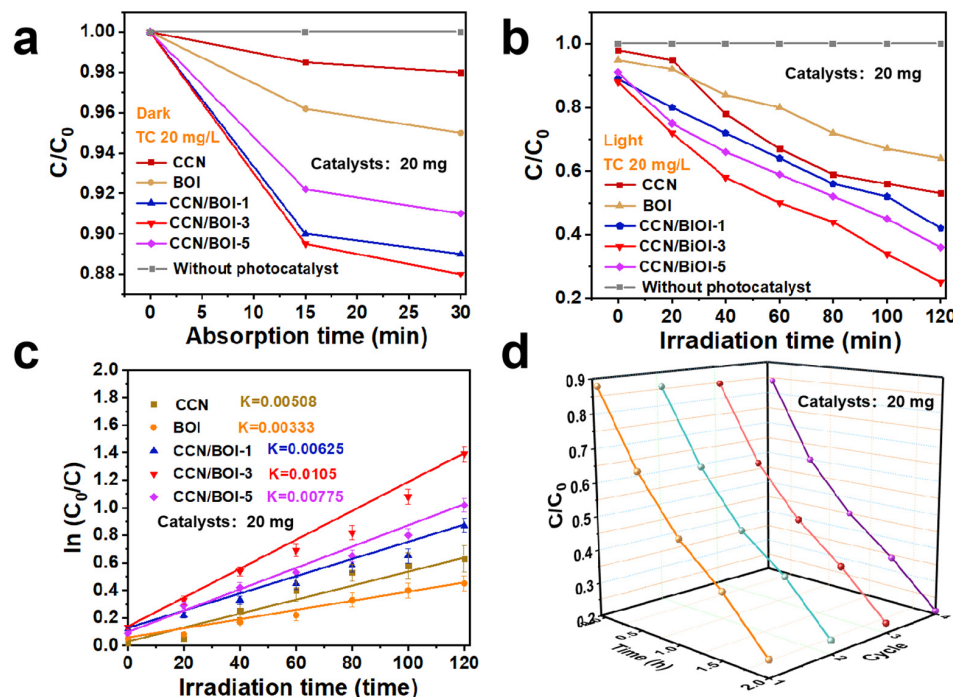


Figure 4. (a) Photodegradation of TC over different catalysts on (a) dark adsorption and (b) light irradiation. (c) The corresponding pseudo-first-order reaction kinetics diagram of as-prepared samples. (d) Photocatalytic degradation cycling runs experiment of CCN/BOI-3 sample.

It can be observed that the CCN/BOI-3 composite exhibited the highest apparent reaction rate constant k values (0.0105 min^{-1}), which are higher than those of pure BOI (0.00333 min^{-1}) and CCN (0.00508 min^{-1}), respectively (Figure 4c). Simultaneously, the photocatalytic degradation activity of CCN/BOI-3 has not been changed significantly after four cycles of reaction (Figure 4d), which indicates that the CCN/BOI composite photocatalyst possesses favorable photocatalytic recycling stability. Furthermore, CCN/BOI-3 materials were employed to degrade other antibiotics such as oxytetracycline (OTC), streptomycin (STR), chlortetracycline (CTC), ciprofloxacin (CIP), and amoxicillin (AMX) under the same conditions (Figure S7), which demonstrated the universality of CCN/BOI-3 for the degradation of antibiotic contaminants.

To investigate the charge transfer at the atomic level, the electrostatic potentials of the CCN and BOI surfaces were evaluated based on density functional theory (DFT). From Figure 5a,b, the work function (Φ) was defined as the difference between the vacuum level (E_{vac}) and the Fermi level (E_f), which were calculated to be 5.02 eV and 2.96 eV for CCN and BOI, respectively. When the CCN is in contact with the BOI, electrons are transferred from the BOI to the CCN until the E_f of both compounds reaches the same level. In addition, the charge density difference (CDD) of the CCN/BOI composite was tested to further analyze the charge transfer mechanism (Figure 5c). It is observed that the interface near the CCN is dominated by yellow regions, which indicates that the BOI loses electrons, while the CCN gains electrons when the CCN/BOI heterojunction is formed. In addition, CCN does not bind to BOI at the interface, indicating that the CCN/BOI heterojunction is a VDW heterojunction [61]. The CCN/BOI VDW heterojunction promotes large interactions at the interface, which is advantageous for achieving fast charge transfer to boost photocatalytic activity. Bard charge analysis confirmed that the electron transfer of approximately 0.3 eV from BOI to CCN at the interface promoted the formation of an intrinsic electric field (IEF), driving the involvement of photogenerated electrons in the photocatalytic degradation process.

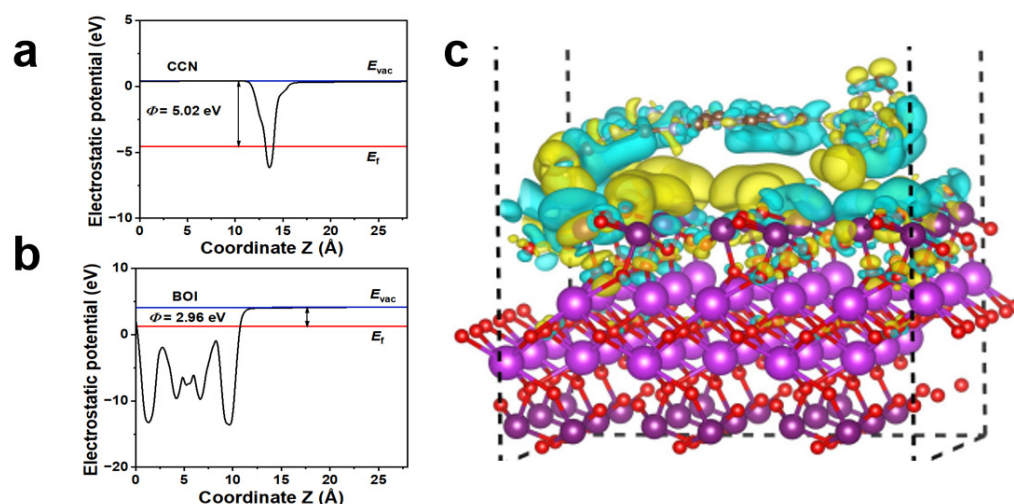


Figure 5. Work function profiles of (a) BOI and (b) CCN. (c) The charge density difference of CCN/BOI heterojunction.

Before elucidating the degradation mechanism of the TC contaminants, the redox capacity and charge transfer pathways of the as-prepared CCN/BOI photocatalyst should be investigated. The energy band structures of CCN and BOI are given in Figure 6a, derived from the UV-vis DRS, work functions, and Mott–Schottky curves. Because the work function of CCN is higher than that of BOI, when the layered BOI is connected to the CCN nanosheet to form a VDW heterojunction, the electrons of BOI are transferred to the layered CCN with higher E_f . As a result, the CCN interface becomes negatively charged by accepting electrons, while the layered BOI interface becomes positively charged by consuming electrons [62]. Furthermore, an IEF pointing from the laminar BOI to the lamellar CCN is

established (Figure 6b). Because both CCN and BOI are UV-vis-responsive semiconductors, electrons could move two parts from VB to CBs in the CCN/BOI heterojunction under the irradiation (Figure 6c). Subsequently, the IEF drives the photoexcited electrons on the CB of the weakly reducing CCN to combine with the photoexcited holes on the VB of the weakly oxidizing BOI. In this way, the strong photoexcited holes and electrons of the CCN/BOI composite are retained, leading to the formation of an S-scheme heterojunction [63]. Moreover, the charge transfer at the heterojunction interface was visualized with Kelvin Probe Force Microscopy (KPFM) measurements (Figure 6d–g). It was observed that the potential of the CCN was 1.34 μV higher than that of the BOI in the absence of light. In contrast, the surface potential of the CCN decreased and that of the BOI increased after 5 min of irradiation, which indicates that the electrons were clustered on the CCN and holes on the BOI at the surface of the heterojunction. The experimental results demonstrate the IEF generation and confirm the charge separation path of the S-scheme heterojunction.

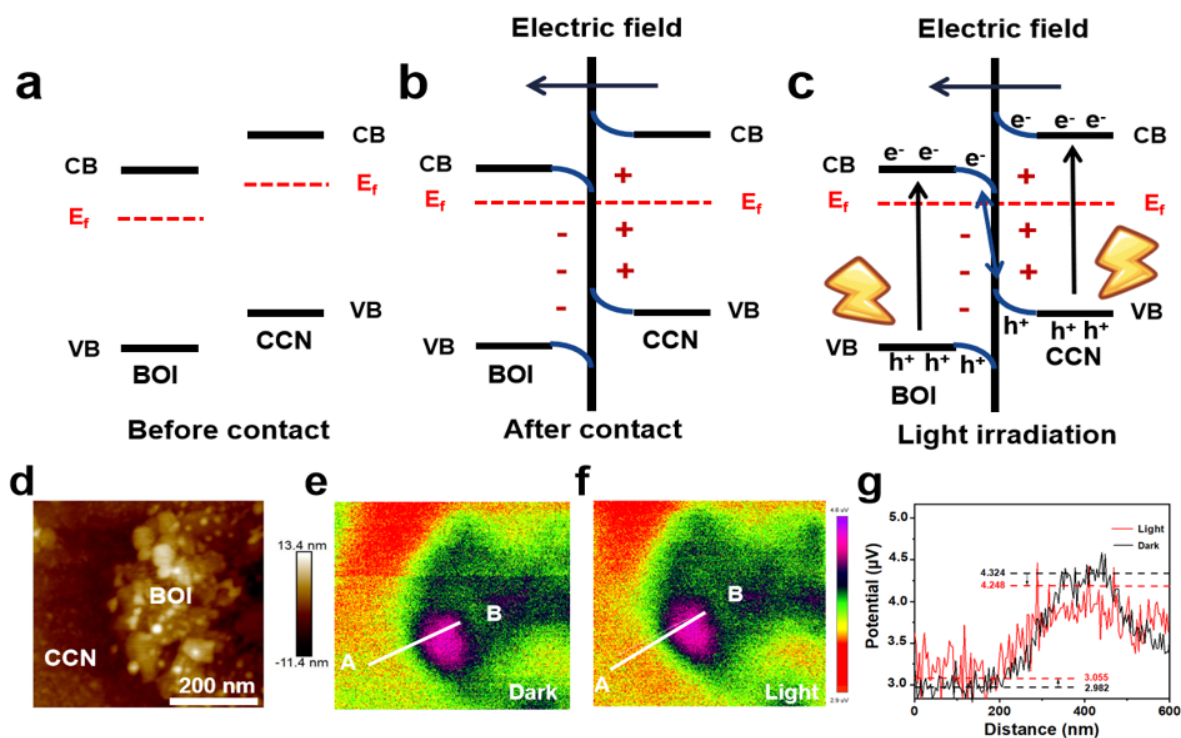


Figure 6. (a) Band configuration of CCN and BOI. (b) Establishment IEF of CCN/BOI heterojunction interface. (c) Photoexcited charge transfer of CCN/BOI S-scheme heterojunction. (d) AFM image of CCN/BOI. KPFM potential images of CCN/BOI (e) in the dark and (f) under light irradiation and (g) the corresponding surface potential curves (correspond to the line from point A to B).

To investigate the charge separation capability of the as-synthesized photocatalysts, photocurrent response curves and electrochemical impedance spectroscopy (EIS) tests were performed [64]. As given in Figure 7a, the photocurrent density is in the order of $\text{CCN/BOI-3} > \text{CCN/BOI-5} > \text{CCN/BOI-1} > \text{BOI} > \text{CCN}$. Apparently, the photocurrent intensity of the CCN/BOI-3 sample is higher than that of the CCN and BOI, indicating that the S-scheme VDW heterojunction can accelerate the separation and migration efficiency of photogenerated electron-hole pairs. Simultaneously, the Nyquist plot reflects the impedance corresponding to the photoexcited charge transfer. In general, the strong resistance to charge transfer leads to a larger arc radius of the semicircle in the Nyquist diagram [65]. It is observed that the arc radius of the CCN/BOI composites is significantly smaller than that of the pristine CCN and BOI, which implies that the S-scheme 2D/2D VDW heterojunction can accelerate the photoinduced charge carrier transfer (Figure 7b). In order to gain insight into the mechanism of enhanced photocatalytic performance, the process of charge transfer was investigated. Initially, exciton dissociation is the main step to generate

free charges [66]. Photoluminescence (PL) spectra and corresponding time-resolved PL spectra were employed to study the dynamics of exciton dissociation generated by photo-excitation in the synthesized photocatalysts. As displayed in Figure 7c, the PL intensity of the CCN/BOI-3 composite is significantly lower compared to that of the pure CCN and BOI, suggesting that the construction of S-scheme VDW heterojunctions plays an important role in suppressing the photogenerated electron-hole pair recombination. Moreover, the corresponding time-resolved PL spectra are shown in Figure 7d. The fluorescence lifetime of CCN/BOI-3 can be calculated to be 3.59 ns, which is lower than that of CCN (3.67 ns) and BOI (3.62 ns), indicating that the S-scheme VDW heterojunction could effectively enhance the dissociation of excitons.

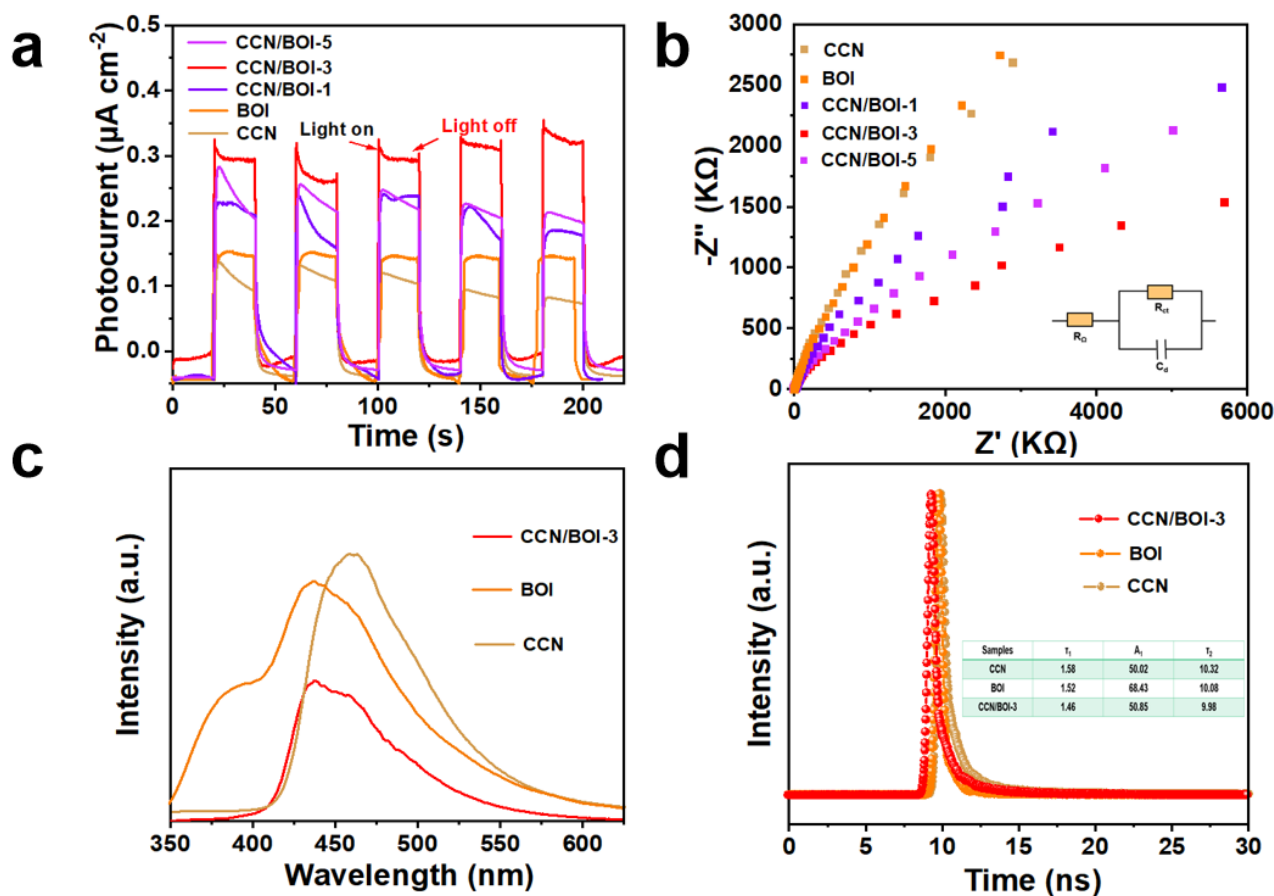


Figure 7. (a) Transient time-photocurrent curves and (b) EIS plots of as-prepared samples. (c) PL and (d) time-resolved PL spectra of CCN, BOI, and CCN/BOI heterojunction.

In order to investigate the degradation pathway of TC, the degradation intermediates of TC were detected by liquid chromatography-mass spectrometry (LC-MS) analysis, and the results are displayed in Figure S4. An intense anionic absorption peak can be observed at $m/z = 445$, which is assigned to the deprotonated TC molecule [67]. As the reaction time increase, the peaks of the TC molecule gradually decrease and some new peaks belonging to the intermediate appeared. A series of degradation products can be identified in the MS spectra, such as $m/z = 465$, 481, 455, 433, 409, 342, and 242. Based on the detected intermediates, the possible degradation pathways of TC were analyzed and are exhibited in Figure 8. Initially, the TC molecules are oxidized by hydroxyl radicals, thus producing the intermediates T1 ($m/z = 465$). T1 is further oxidized by the hydroxyl groups to T2 ($m/z = 481$). By loss of the N-methyl group, product T2 is further converted to compound T3 ($m/z = 455$), with subsequent loss of amino leading to the formation of compounds T4 ($m/z = 433$). T5 ($m/z = 409$) is formed by T4 removing the c functional group [5]. The gradual separation of the branched chain groups of T5 forms T6 ($m/z = 345$), and after continuous

redox reaction, opens the six-element ring structure to form T7 ($m/z = 242$). Finally, with the extension of the irradiation time, all intermediates are further degraded to H_2O , NH_4^+ , and CO_2 , etc. [68].

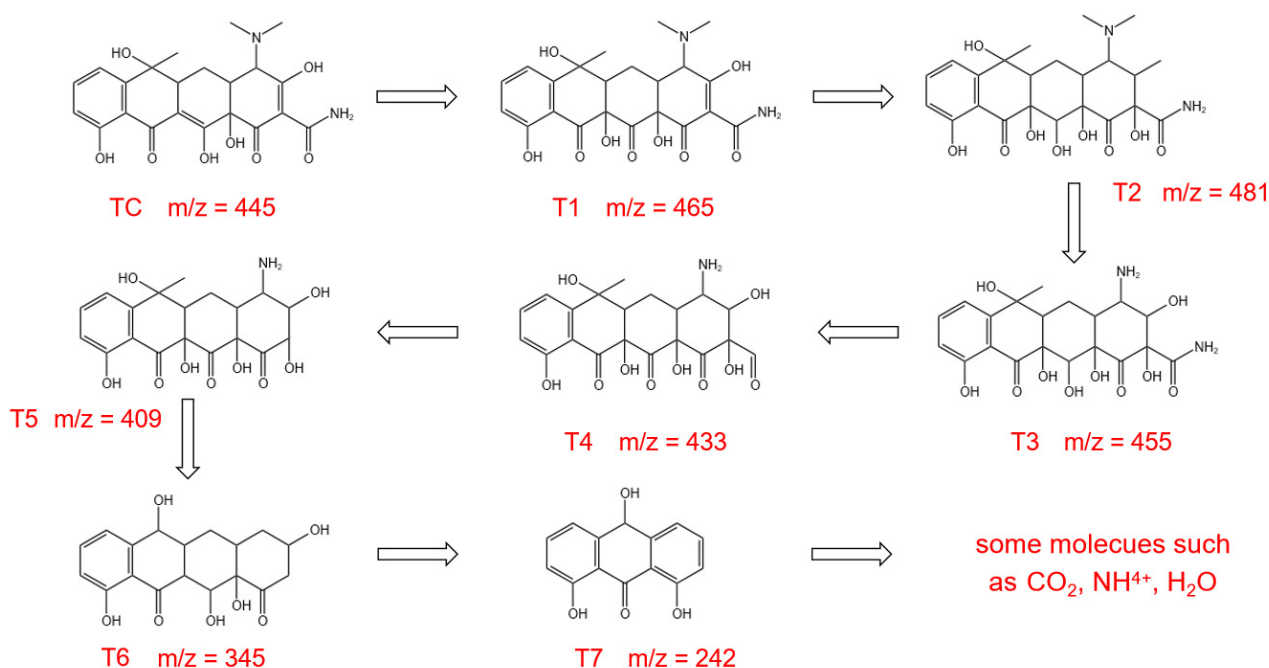


Figure 8. Possible photocatalytic degradation pathways of TC over CCN/BOI heterojunction.

The biotoxicity of the TC solution after photocatalysis has attracted much attention due to its negative effects on the daily environment. Mung bean sprouts were cultured in different solution systems to explore the changes of TC biotoxicity before and after photocatalytic degradation. First, mung bean sprout seeds were planted in petri dishes containing deionized water, TC solution, and photocatalyst-treated TC solution, respectively, and the pictures after seven days of planting are presented in Figure 9. From Figure 9a, it can be observed that all bean sprouts grown in deionized water germinated successfully and grew well. In contrast, the mung beans grown in untreated TC solution germinated successfully but grew poorly (Figure 9b). Surprisingly, all mung beans in the treated TC solution germinated as it was in an aqueous solution (Figure 9c), indicating that the photocatalyst degraded most of the biotoxic molecules, and the biotoxicity of the treated TC solution was significantly reduced. In addition, mung bean sprouts grown in the photocatalyst-treated TC solution were slightly worse than those grown in deionized water, which was mainly due to a small fraction of residual TC toxicity in the water [69].



Figure 9. Growth of mung beans in different solutions: (a) control; (b) TC solution; and (c) TC solution after photocatalysis.

Based on the above experimental results and theoretical calculation analysis, the possible photocatalytic TC degradation mechanism of S-scheme CCN/BOI VDW heterojunctions is presented in Figure 10. DFT calculations indicate that the Fermi level of CCN is higher than that of BOI. Consequently, upon material contact, electrons tend to spontaneously migrate from BOI to CCN until the Fermi level reaches equilibrium. The charge rearrangement process leads to band-edge bending, creating an established IEF at the interface between the CCN and the BOI. Under visible light and irradiation, the CCN and BOI materials are excited to generate electrons and holes. With the built-in electric field, electrons in BOI CB readily recombine with holes on CCN VB, leading to electron transfer along the path of the S-scheme. Furthermore, the strong interaction between the 2D CCN and BOI nanosheets can promote charge transfer and facilitate the rearrangement of energy level, which has been demonstrated by the M–S diagram. As displayed in Figure S5, the CCN/BOI material exhibits a lower positive slope of the curve than that of CCN and BOI, indicating an enhanced concentration of charge carriers in the VDW heterostructure [70]. Furthermore, the holes on the VB of BOI could trap free OH[−] in water and further oxidize it to hydroxy radicals (OH) [71]. Meanwhile, the electrons accumulated on the CB of CCN can continuously reduce O₂ to superoxide radical (O₂[−]) [72]. Moreover, distinctive peaks for DMPO·OH and DMPO·O₂[−] can be detected during the photocatalytic reaction via electron spin resonance (ESR) measurements, confirming the presence of ·OH and ·O₂[−] active species (Figure S6). Ultimately, the major active substances are able to oxidatively reduce TC to H₂O, CO₂, etc. The reaction mechanism of CCN/BOI photocatalytic degradation of TC can be summarized as follows:

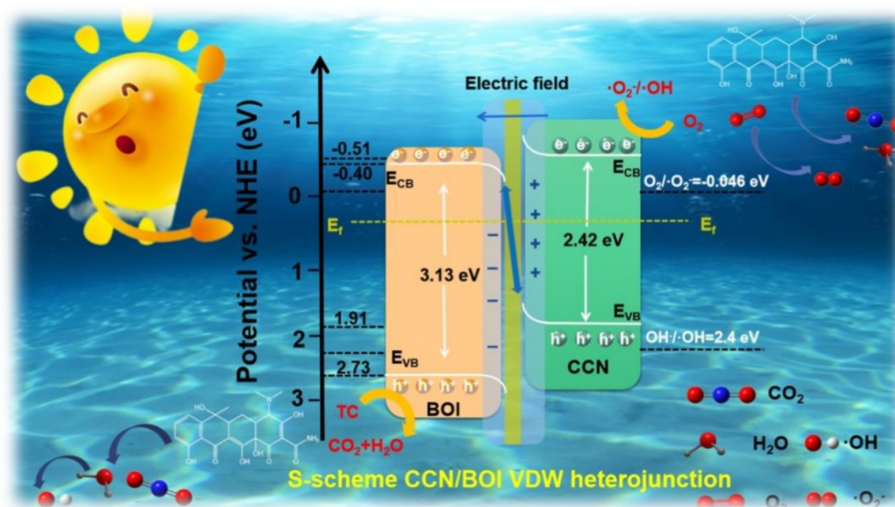
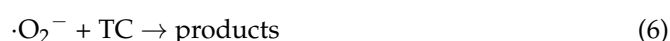
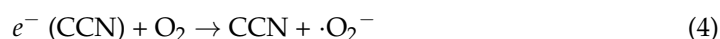
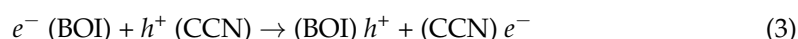
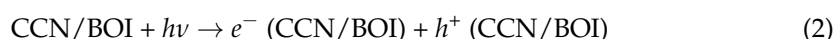


Figure 10. Proposed photocatalytic reaction mechanism for the degradation of TC over CCN/BOI heterojunction.

3. Materials and Methods

3.1. Chemical Reagents

Melamine ($C_3N_3(NH_2)_3$), bismuth nitrate pentahydrate ($Bi(NO_3)_3 \cdot 5H_2O$), nitric acid (HNO_3), and potassium iodate (KIO_3) were all analytical-grade reagents and purchased from Sinopharm Reagent Co., Ltd (Shanghai, China). The tetracycline used for the experiment was purchased from Aladdin Reagent Co., Ltd (Shanghai, China).

3.2. Synthesis of Crystalline CN (CCN) Nanosheets

Crystalline carbon nitride (CCN) was prepared based on a previously reported one-step rapid polymerization strategy [73]. A certain amount of melamine (3 g) was placed in a crucible and calcined directly at 550 °C in a muffle furnace for 4 h. Finally, the temperature was reduced to room temperature (the cooling rate was 10 °C/min) and yellow powder was obtained by grinding as CCN. For comparison, the bulk g- C_3N_4 was fabricated by calcinating 10 g melamine at 500 °C in a muffle furnace for 4 h (heating rate: 10 °C/min) with a covered crucible. After cooling down, the collected yellow sample was ground to powder and denoted as BCN.

3.3. Synthesis of $BiOIO_3$ (BOI) Nanosheets

The flake $BiOIO_3$ was prepared by a hydrothermal procedure. A quantity of $Bi(NO_3)_3 \cdot 5H_2O$ (1.0 g) and KIO_3 (0.4 g) were dissolved in 60 mL of pure water under continuous stirring for 30 min, with the addition of 2 mL HNO_3 solution. Subsequently, the mixed suspension was transferred to a 100-mL Teflon-lined autoclave and heated at 150 °C for 15 h. The obtained $BiOIO_3$ product was then washed three times with pure water and ethanol, before drying in an oven at 60 °C for 8 h and being denoted as BOI.

3.4. Synthesis of CCN/BOI Heterojunctions

For the synthesis of the CCN/BOI composites, 1.0 g $Bi(NO_3)_3 \cdot 5H_2O$ and 2 mL HNO_3 were added to 60 mL of pure water then stirred for 15 min. Subsequently, a quantity of CCN and 0.4 g KIO_3 were added to the above mixture under continuous magnetic stirring for 30 min. The suspension was then transferred to a 100-mL Teflon-lined autoclave and heated at 150 °C for 15 h. After cooling to room temperature, the product was centrifuged and washed several times with water and ethanol, respectively. Finally, the processed product was dried in an oven at 60 °C for 8 h. For comparison, the CCN/BOI preparation was supplemented with 1, 3, and 5 wt.% of CCN content. For convenience, the resulting complexes are recorded as CCN-BOI-1, CCN-BOI-3, and CCN-BOI-5, respectively.

4. Conclusions

In summary, the 2D/2D S-scheme CCN/BOI van der Waals heterojunction was successfully fabricated via a simple hydrothermal method. The 2D/2D structured CCN/BOI allows the synthesized photocatalysts to possess a large interface area, providing a channel for charge transfer, while the van der Waals force between the components accelerates carrier separation and transfer. Furthermore, the S-scheme heterojunctions enhance the redox ability of 2D/2D CCN/BOI composites, contributing a significant driving force for subsequent photocatalytic degradation of TC. As expected, the as-synthesized optimal CCN/BOI-3 photocatalyst displayed an excellent degradation performance and an outstanding TC degradation rate within 120 min, which is 2 times and 2.7 times higher than that of pure CCN and BOI, respectively. This work provides guidance for the design of efficient photocatalysts with 2D/2D S-scheme van der Waals heterojunctions.

Supplementary Materials: The following supporting information can be downloaded at: <https://www.mdpi.com/article/10.3390/molecules28135098/s1>, Figure S1 (a) SEM image of CCN/BOI-3 and (b) EDS spectrum of CCN/BOI-3. Figure S2 XRD patterns of BCN and CCN. Figure S3 Digital photographs of (a) CCN, (b) BOI, (c) CCN/BOI-1, (d) CCN/BOI-3, (e) CCN/BOI-5. Figure S4 LC-MS spectra of possible intermediates for the degradation of TC over CCN/BOI heterojunction.

Figure S5 M-S plots of CCN, BOI and CCN/BOI-3. Figure S6 ESR spectra of the (a) DMPO-•OH and (b) DMPO-•O₂⁻ over CCN/BOI in the dark and under visible light irradiation. Figure S7 Degradation rates of CCN/BOI-3 photocatalysts for different kinds of antibiotics: tetracycline (TC), oxytetracycline (OTC), streptomycin (STR), chlortetracycline (CTC), ciprofloxacin (CIP) and amoxicillin (AMX) at concentrations of 20 mg/L. Table S1 Comparison of CCN/BOI reaction systems photocatalytic performance with other previously reported reaction systems [74–79].

Author Contributions: Software, X.D.; Formal analysis, Y.S.; Data curation, L.C. and Z.C.; Writing—original draft, X.K. and L.C.; Writing—review & editing, W.S. All authors have read and agreed to the published version of the manuscript.

Funding: National Natural Science Foundation of China: 22006057.

Institutional Review Board Statement: Not applicable.

Informed Consent Statement: Not applicable.

Data Availability Statement: Not applicable.

Acknowledgments: The authors would like to acknowledge the funding support from the National Natural Science Foundation of China (No. 22006057 and 21908115) and “Doctor of Mass entrepreneurship and innovation” Project in Jiangsu Province.

Conflicts of Interest: The authors declare no conflict of interest.

Sample Availability: Samples of the compounds are available or not available from the authors.

References

1. Wang, H.; Li, J.; Zhou, M.; Guan, Q.; Lu, Z.; Huo, P.; Yan, Y. Preparation and characterization of Ag₂O/SWNTs photocatalysts and its photodegradation on tetracycline. *J. Ind. Eng. Chem.* **2015**, *30*, 64–70. [CrossRef]
2. Delgado, N.; Bermeo, L.; Hoyos, D.A.; Peñuela, G.A.; Capparelli, A.; Marino, D.; Navarro, A.; Casas-Zapata, J.C. Occurrence and removal of pharmaceutical and personal care products using subsurface horizontal flow constructed wetlands. *Water Res.* **2020**, *187*, 116448. [CrossRef] [PubMed]
3. Chen, F.; Ma, T.; Zhang, T.; Zhang, Y.; Huang, H. Atomic-Level Charge Separation Strategies in Semiconductor-Based Photocatalysts. *Adv. Mater.* **2021**, *33*, e2005256. [CrossRef] [PubMed]
4. Nemiwal, M.; Zhang, T.C.; Kumar, D. Recent progress in g-C₃N₄, TiO₂ and ZnO based photocatalysts for dye degradation: Strategies to improve photocatalytic activity. *Sci. Total Environ.* **2021**, *767*, 144896. [CrossRef]
5. Shen, H.; Wang, J.; Jiang, J.; Luo, B.; Mao, B.; Shi, W. All-solid-state Z-scheme system of RGO-Cu₂O/Bi₂O₃ for tetracycline degradation under visible-light irradiation. *Chem. Eng. J.* **2017**, *313*, 508–517. [CrossRef]
6. Nasir, J.A.; Rehman, Z.-U.; Shah, S.N.A.; Khan, A.; Butler, I.S.; Catlow, C.R.A. Recent developments and perspectives in CdS-based photocatalysts for water splitting. *J. Mater. Chem. A* **2020**, *8*, 20752–20780. [CrossRef]
7. Gao, P.; Yang, Y.; Yin, Z.; Kang, F.; Fan, W.; Sheng, J.; Feng, L.; Liu, Y.; Du, Z.; Zhang, L. A critical review on bismuth oxyhalide based photocatalysis for pharmaceutical active compounds degradation: Modifications, reactive sites, and challenges. *J. Hazard. Mater.* **2021**, *412*, 125186. [CrossRef]
8. Wu, Q.; Li, Z.; Hong, H. Adsorption of the quinolone antibiotic nalidixic acid onto montmorillonite and kaolinite. *Appl. Clay Sci.* **2012**, *74*, 66–73. [CrossRef]
9. Shi, Y.; Li, L.; Xu, Z.; Guo, F.; Li, Y.; Shi, W. Synergistic coupling of piezoelectric and plasmonic effects regulates the Schottky barrier in Ag nanoparticles/ultrathin g-C₃N₄ nanosheets heterostructure to enhance the photocatalytic activity. *Appl. Surf. Sci.* **2023**, *616*, 156466. [CrossRef]
10. Sun, H.; Guo, F.; Pan, J.; Huang, W.; Wang, K.; Shi, W. One-pot thermal polymerization route to prepare N-deficient modified g-C₃N₄ for the degradation of tetracycline by the synergistic effect of photocatalysis and persulfate-based advanced oxidation process. *Chem. Eng. J.* **2020**, *406*, 126844. [CrossRef]
11. Guo, F.; Shi, C.; Sun, W.; Liu, Y.; Lin, X.; Shi, W. Pomelo biochar as an electron acceptor to modify graphitic carbon nitride for boosting visible-light-driven photocatalytic degradation of tetracycline. *Chin. J. Chem. Eng.* **2021**, *48*, 1–11. [CrossRef]
12. Shi, Y.; Li, L.; Xu, Z.; Sun, H.; Guo, F.; Shi, W. One-step simple green method to prepare carbon-doped graphitic carbon nitride nanosheets for boosting visible-light photocatalytic degradation of tetracycline. *J. Chem. Technol. Biotechnol.* **2021**, *96*, 3122–3133. [CrossRef]
13. Cao, D.; Wang, X.; Zhang, H.; Yang, D.; Yin, Z.; Liu, Z.; Lu, C.; Guo, F. Rational Design of Monolithic g-C₃N₄ with Floating Network Porous-like Sponge Monolithic Structure for Boosting Photocatalytic Degradation of Tetracycline under Simulated and Natural Sunlight Illumination. *Molecules* **2023**, *28*, 3989. [CrossRef] [PubMed]
14. Guo, F.; Chen, Z.; Huang, X.; Cao, L.; Cheng, X.; Shi, W.; Chen, L. Cu₃P nanoparticles decorated hollow tubular carbon nitride as a superior photocatalyst for photodegradation of tetracycline under visible light. *Sep. Purif. Technol.* **2021**, *275*, 119223. [CrossRef]

15. Shi, W.; Cao, L.; Shi, Y.; Chen, Z.; Cai, Y.; Guo, F.; Du, X. Environmentally friendly supermolecule self-assembly preparation of S-doped hollow porous tubular g-C₃N₄ for boosted photocatalytic H₂ production. *Ceram. Int.* **2023**, *49*, 11989–11998. [[CrossRef](#)]
16. Shi, W.; Liu, Y.; Sun, W.; Hong, Y.; Li, X.; Lin, X.; Guo, F.; Shi, J. Assembling g-C₃N₄ nanosheets on rod-like CoFe₂O₄ nanocrystals to boost photocatalytic degradation of ciprofloxacin with peroxymonosulfate activation. *Mater. Today Commun.* **2021**, *29*, 102871. [[CrossRef](#)]
17. Yuan, H.; Shi, W.; Lu, J.; Wang, J.; Shi, Y.; Guo, F.; Kang, Z. Dual-channels separated mechanism of photo-generated charges over semiconductor photocatalyst for hydrogen evolution: Interfacial charge transfer and transport dynamics insight. *Chem. Eng. J.* **2023**, *454*, 140442. [[CrossRef](#)]
18. Guo, F.; Chen, Z.; Huang, X.; Cao, L.; Cheng, X.; Shi, W.; Chen, L. Ternary Ni₂P/Bi₂MoO₆/g-C₃N₄ composite with Z-scheme electron transfer path for enhanced removal broad-spectrum antibiotics by the synergistic effect of adsorption and photocatalysis. *Chin. J. Chem. Eng.* **2022**, *44*, 157. [[CrossRef](#)]
19. Guo, F.; Huang, X.; Chen, Z.; Cao, L.; Cheng, X.; Chen, L.; Shi, W. Construction of Cu₃P-ZnSnO₃-g-C₃N₄ p-n-n heterojunction with multiple built-in electric fields for effectively boosting visible-light photocatalytic degradation of broad-spectrum antibiotics. *Sep. Purif. Technol.* **2021**, *265*, 118477. [[CrossRef](#)]
20. Zhang, W.; Shi, W.; Sun, H.; Shi, Y.; Luo, H.; Jing, S.; Fan, Y.; Guo, F.; Lu, C. Fabrication of ternary CoO/g-C₃N₄/Co₃O₄ nanocomposite with p-n-p type heterojunction for boosted visible-light photocatalytic performance. *J. Chem. Technol. Biotechnol.* **2021**, *96*, 1854. [[CrossRef](#)]
21. Zhu, X.; Guo, F.; Pan, J.; Sun, H.; Gao, L.; Deng, J.; Zhu, X.; Shi, W. Fabrication of visible-light-response face-contact ZnSnO₃@g-C₃N₄ core-shell heterojunction for highly efficient photocatalytic degradation of tetracycline contaminant and mechanism insight. *J. Mater. Sci.* **2020**, *56*, 4366–4379. [[CrossRef](#)]
22. Shi, W.; Cao, L.; Shi, Y.; Zhong, W.; Chen, Z.; Wei, Y.; Guo, F.; Chen, L.; Du, X. Boosted built-in electric field and active sites based on Ni-doped heptazine/triazine crystalline carbon nitride for achieving high-efficient photocatalytic H₂ evolution. *J. Mol. Struct.* **2023**, *1280*, 135076. [[CrossRef](#)]
23. Shi, W.; Yang, S.; Sun, H.; Wang, J.; Lin, X.; Guo, F.; Shi, J. Carbon dots anchored high-crystalline g-C₃N₄ as a metal-free composite photocatalyst for boosted photocatalytic degradation of tetracycline under visible light. *J. Mater. Sci.* **2020**, *56*, 2226–2240. [[CrossRef](#)]
24. Xu, Z.; Shi, Y.; Li, L.; Sun, H.; Amin, S.; Guo, F.; Wen, H.; Shi, W. Fabrication of 2D/2D Z-scheme highly crystalline carbon nitride/ δ -Bi₂O₃ heterojunction photocatalyst with enhanced photocatalytic degradation of tetracycline. *J. Alloys Compd.* **2021**, *895*, 162667. [[CrossRef](#)]
25. Iqbal, W.; Qiu, B.; Zhu, Q.; Xing, M.; Zhang, J. Self-modified breaking hydrogen bonds to highly crystalline graphitic carbon nitrides nanosheets for drastically enhanced hydrogen production. *Appl. Catal. B Environ.* **2018**, *232*, 306–313. [[CrossRef](#)]
26. Wang, Z.; Chen, Y.; Zhang, L.; Cheng, B.; Yu, J.; Fan, J. Step-scheme CdS/TiO₂ nanocomposite hollow microsphere with enhanced photocatalytic CO₂ reduction activity. *J. Mater. Sci. Technol.* **2020**, *56*, 143–150. [[CrossRef](#)]
27. Xie, Y.; Shang, X.; Liu, D.; Zhao, H.; Gu, Y.; Zhang, Z.; Wang, X. Non-noble metal thickness-tunable Bi₂MoO₆ nanosheets for highly efficient visible-light-driven nitrobenzene reduction into aniline. *Appl. Catal. B Environ.* **2019**, *259*, 118087. [[CrossRef](#)]
28. Shi, W.; Li, M.; Huang, X.; Ren, H.; Yan, C.; Guo, F. Facile synthesis of 2D/2D Co₃(PO₄)₂/g-C₃N₄ heterojunction for highly photocatalytic overall water splitting under visible light. *Chem. Eng. J.* **2020**, *382*, 122960. [[CrossRef](#)]
29. Wang, L.; Xue, Y.; Yang, G.; Liu, X.; He, W.; Zhang, M.; Liu, Z. Electronic structure regulation of an S-scheme CuBi₂O₄/Sr_{0.5}NaTaO₃ heterojunction with efficient carrier spatial transfer. *Sep. Purif. Technol.* **2023**, *317*, 123856. [[CrossRef](#)]
30. Chen, K.; Shi, Y.; Shu, P.; Luo, Z.; Shi, W.; Guo, F. Construction of core-shell FeS₂@ZnIn₂S₄ hollow hierarchical structure S-scheme heterojunction for boosted photothermal-assisted photocatalytic H₂ production. *Chem. Eng. J.* **2023**, *454*, 140053. [[CrossRef](#)]
31. Lu, C.; Wang, J.; Cao, D.; Guo, F.; Hao, X.; Li, D.; Shi, W. Synthesis of magnetically recyclable g-C₃N₄/NiFe₂O₄ S-scheme heterojunction photocatalyst with promoted visible-light-response photo-Fenton degradation of tetracycline. *Mater. Res. Bull.* **2023**, *158*, 112064. [[CrossRef](#)]
32. Shi, W.; Fu, Y.; Sun, H.; Sun, X.; Hao, C.; Guo, F.; Tang, Y. Construction of 0D/3D CoFe₂O₄/MIL-101(Fe) complement each other S-scheme heterojunction for effectively boosted photocatalytic degradation of tetracycline. *Inorg. Chem. Commun.* **2022**, *146*, 110140. [[CrossRef](#)]
33. Wang, L.; Niu, M.; Liu, Y.; Xie, Y.; Ma, Z.; Zhang, M.; Hou, C. The Ovs surface defecting of an S-scheme g-C₃N₄/H₂Ti₃O₇ nanoheterostructures with accelerated spatial charge transfer. *J. Colloid Interface Sci.* **2023**, *645*, 639. [[CrossRef](#)] [[PubMed](#)]
34. Shi, W.; Sun, W.; Liu, Y.; Li, X.; Lin, X.; Guo, F.; Hong, Y. Onion-ring-like g-C₃N₄ modified with Bi₃TaO₇ quantum dots: A novel 0D/3D S-scheme heterojunction for enhanced photocatalytic hydrogen production under visible light irradiation. *Renew. Energy* **2021**, *182*, 958–968. [[CrossRef](#)]
35. Shi, Y.; Li, L.; Xu, Z.; Guo, F.; Shi, W. Construction of full solar-spectrum available S-scheme heterojunction for boosted photothermal-assisted photocatalytic H₂ production. *Chem. Eng. J.* **2023**, *459*, 141549. [[CrossRef](#)]
36. Wang, J.; Shi, Y.; Sun, H.; Shi, W.; Guo, F. Fabrication of Bi₄Ti₃O₁₂/ZnIn₂S₄ S-scheme heterojunction for achieving efficient photocatalytic hydrogen production. *J. Alloys Compd.* **2023**, *930*, 167450. [[CrossRef](#)]
37. Wang, L.; Liu, Y.; Hao, J.; Ma, Z.; Lu, Y.; Zhang, M.; Hou, C. Construction of an S-scheme TiOF₂/HTiOF₃ heterostructures with abundant OVs and OH groups: Performance, kinetics and mechanism insight. *J. Colloid Interface Sci.* **2023**, *640*, 15. [[CrossRef](#)]

38. Xu, Z.; Shi, W.; Shi, Y.; Sun, H.; Li, L.; Guo, F.; Wen, H. Carbon dots as solid-state electron mediator and electron acceptor in S-scheme heterojunction for boosted photocatalytic hydrogen evolution. *Appl. Surf. Sci.* **2022**, *595*, 153482. [[CrossRef](#)]
39. Wang, Y.; Zhu, X.R.; Li, Y.F. Spin-orbit coupling-dominated catalytic activity of twodimensional bismuth toward CO₂ electro-reduction: Not the thinner the better. *J. Phys. Chem. Lett.* **2019**, *10*, 4663–4667. [[CrossRef](#)]
40. Wang, B.B.; Chen, D.Y.; Li, N.J.; Xu, Q.F.; Li, H.; He, J.H.; Lu, J.M. Z-scheme photocatalytic NO removal on a 2D/2D iodine doped BiOIO₃/g-C₃N₄ under visiblelight irradiation. *J. Colloid Interface Sci.* **2020**, *576*, 426–434. [[CrossRef](#)]
41. Wang, T.; He, S.F.; Zhang, Y.S.; Wang, J.W.; Pan, W.P. Photocatalytic removal of elemental mercury on TiO₂-BiOIO₃ heterostructures: Mercury transformation, sulfur tolerance and SO₂/SO₃ conversion. *Chem. Eng. J.* **2020**, *388*, 124390. [[CrossRef](#)]
42. Shifa, T.A.; Wang, F.; Liu, Y.; He, J. Heterostructures Based on 2D Materials: A Versatile Platform for Efficient Catalysis. *Adv. Mater.* **2018**, *31*, e1804828. [[CrossRef](#)]
43. Lai, J.; Jiang, X.; Zhao, M.; Cui, S.; Yang, J.; Li, Y. Thickness-dependent layered BiOIO₃ modified with carbon quantum dots for photodegradation of bisphenol A: Mechanism, pathways and DFT calculation. *Appl. Catal. B Environ.* **2021**, *298*, 120622. [[CrossRef](#)]
44. Xing, W.N.; Tu, W.G.; Han, Z.H.; Hu, Y.D.; Meng, Q.Q.; Chen, G. Template-induced high-crystalline g-C₃N₄ nanosheets for enhanced photocatalytic H₂ evolution. *ACS Energy Lett.* **2018**, *3*, 514–519. [[CrossRef](#)]
45. Liu, G.; Xue, M.; Liu, Q.; Yang, H.; Zhou, Y. Facile synthesis of C-doped hollow spherical g-C₃N₄ from supramolecular self-assembly for enhanced photoredox water splitting. *Int. J. Hydrogen Energy* **2019**, *44*, 25671–25679. [[CrossRef](#)]
46. Gao, H.L.; Yan, S.C.; Wang, J.J.; Huang, Y.A.; Wang, P.; Li, Z.S. Toward efficient solar hydrogen production by intercalated carbon nitride photocatalyst. *Phys. Chem. Chem. Phys.* **2013**, *15*, 18077–18084. [[CrossRef](#)] [[PubMed](#)]
47. Chen, F.; Huang, H.W.; Zeng, C.; Du, X.; Zhang, Y.H. Achieving enhanced UV and visible light photocatalytic activity for ternary Ag/AgBr/BiOIO₃: Decomposition for diverse industrial contaminants with distinct mechanisms and complete mineralization ability. *ACS Sustain. Chem. Eng.* **2017**, *5*, 7777–7791. [[CrossRef](#)]
48. Su, L.X.; Liu, Z.Y.; Ye, Y.L.; Shen, C.L.; Lou, Q.; Shan, C.X. Heterostructured boron doped nanodiamonds@g-C₃N₄ nanocomposites with enhanced photocatalytic capability under visible light irradiation. *Int. J. Hydrogen Energy* **2019**, *44*, 19805–19815. [[CrossRef](#)]
49. Jiang, R.R.; Wu, D.H.; Lu, G.H.; Yan, Z.H.; Liu, J.C. Modified 2D-2D ZnIn₂S₄/BiOCl van der Waals heterojunctions with CQDs: Accelerated charge transfer and enhanced photocatalytic activity under vis- and NIR-light. *Chemosphere* **2019**, *227*, 82–92. [[CrossRef](#)]
50. Xie, J.; Cao, Y.L.; Hu, J.D.; Tang, Y.K.; Jia, D.Z. A solvent-free strategy to realize the substitution of I[−] for IO₃[−] in a BiOIO₃ photo-catalyst with an opposite charge transfer path. *Green Chem.* **2020**, *22*, 1424–1431. [[CrossRef](#)]
51. Han, W.Y.; Li, D.G.; Zhang, M.Q.; Hu, X.M.; Duan, X.G.; Liu, S.M. Photocatalytic activation of peroxy monosulfate by surface-tailored carbon quantum dots. *J. Hazard. Mater.* **2020**, *395*, 122695. [[CrossRef](#)]
52. Zhu, C.Z.; Wang, Y.T.; Jiang, Z.F.; Xu, F.C.; Xian, Q.M.; Sun, C. CeO₂ nanocrystal-modified layered MoS₂/g-C₃N₄ as 0D/2D ternary composite for visible-light photocatalytic hydrogen evolution: Interfacial consecutive multi-step electron transfer and enhanced H₂O reactant adsorption. *Appl. Catal. B-Environ.* **2019**, *259*, 118072. [[CrossRef](#)]
53. CBai, P.; Bi, J.C.; Wu, J.B.; Xu, Y.; Wohlrab, S.; Han, Y.D. In-situ solid-phase fabrication of Ag/AgX (X=Cl, Br, I)/g-C₃N₄ composite sites for enhanced visible-light hydrogen evolution. *Int. J. Hydrog. Energy* **2019**, *44*, 21397–21405.
54. Hu, X.; Guo, R.T.; Lin, Z.D.; Bi, Z.X.; Chen, X.; Wang, J.; Pan, W.G. Construction of Carbon Dot-Modified g-C₃N₄/BiOIO₃ Z-Scheme Heterojunction for Boosting Photocatalytic CO₂ Reduction under Full Spectrum Light. *ACS Sustain. Chem. Eng.* **2022**, *10*, 11143–11153. [[CrossRef](#)]
55. Wu, Y.; Li, C.; Liu, W.; Li, H.; Gong, Y.; Niu, L.; Liu, X.; Sun, C.; Xu, S. Unexpected monoatomic catalytic-host synergetic OER/ORR by graphitic carbon nitride: Density functional theory. *Nanoscale* **2019**, *11*, 5064–5071. [[CrossRef](#)] [[PubMed](#)]
56. Li, H.; Wu, Y.; Li, L.; Gong, Y.; Niu, L.; Liu, X.; Wang, T.; Sun, C.; Li, C. Adjustable photocatalytic ability of monolayer g-C₃N₄ utilizing single-metal atom: Density functional theory. *Appl. Surf. Sci.* **2018**, *457*, 735–744. [[CrossRef](#)]
57. Jiang, R.R.; Lu, G.H.; Yan, Z.H.; Wu, D.H.; Zhou, R.R.; Bao, X.H. Insights into a CQD-SnNb₂O₆/BiOCl Z-scheme system for the degradation of benzocaine: Influence factors, intermediate toxicity and photocatalytic mechanism. *Chem. Eng. J.* **2019**, *374*, 79–90. [[CrossRef](#)]
58. Fang, L.J.; Li, Y.H.; Liu, P.F.; Wang, D.P.; Zeng, H.D.; Wang, X.L.; Yang, H.G. Facile Fabrication of Large-Aspect-Ratio g-C₃N₄ Nanosheets for Enhanced Photocatalytic Hydrogen Evolution. *ACS Sustain. Chem. Eng.* **2017**, *5*, 2039–2043. [[CrossRef](#)]
59. Lu, S.; Li, C.; Li, H.H.; Zhao, Y.F.; Gong, Y.Y.; Niu, L.Y. The effects of nonmetal dopants on the electronic, optical and chemical performances of monolayer g-C₃N₄ by first-principles study. *Appl. Surf. Sci.* **2017**, *392*, 966–974. [[CrossRef](#)]
60. Wang, B.; Cheng, L.Y.; Zhang, J.G.; Yu, Y.J.; Li, S.; Wageh, A.; Al-Ghamdi, A. S-Scheme 2D/2D Bi₂MoO₆/BiOI van der Waals heterojunction for CO₂ photoreduction. *Chin. J. Catal.* **2022**, *43*, 1657–1666. [[CrossRef](#)]
61. Li, G.; Lian, Z.; Wan, Z.; Liu, Z.; Qian, J.; Deng, Y.; Zhang, S.; Zhong, Q. Efficient photothermal-assisted photocatalytic NO removal on molecular cobalt phthalocyanine/Bi₂WO₆ Z-scheme heterojunctions by promoting charge transfer and oxygen activation. *Appl. Catal. B Environ.* **2022**, *317*, 121787. [[CrossRef](#)]
62. Cheng, C.; He, B.; Fan, J.; Cheng, B.; Cao, S.; Yu, J. An Inorganic/Organic S-Scheme Heterojunction H₂-Production Photocatalyst and its Charge Transfer Mechanism. *Adv. Mater.* **2021**, *33*, 2100317. [[CrossRef](#)] [[PubMed](#)]

63. Jiang, R.; Wu, D.; Lu, G.; Yan, Z.; Liu, J.; Zhou, R.; Nkoom, M. Fabrication of Fe₃O₄ quantum dots modified BiOCl/BiVO₄ p-n heterojunction to enhance photocatalytic activity for removing broad-spectrum antibiotics under visible light. *J. Taiwan Inst. Chem. Eng.* **2019**, *96*, 681–690. [[CrossRef](#)]
64. Che, H.; Che, G.; Zhou, P.; Liu, C.; Dong, H.; Li, C.; Song, N.; Li, C. Nitrogen doped carbon ribbons modified g-C₃N₄ for markedly enhanced photocatalytic H₂-production in visible to near-infrared region. *Chem. Eng. J.* **2020**, *382*, 122870. [[CrossRef](#)]
65. Wang, J.B.; Liu, C.; Yang, S.; Lin, X.; Shi, W.L. Fabrication of a ternary heterostructure BiVO₄ quantum dots/C60/g-C₃N₄ photo-catalyst with enhanced photocatalytic activity. *J. Phys. Chem. Solids* **2020**, *136*, 10924. [[CrossRef](#)]
66. Hu, Y.; Chen, K.; Li, Y.-L.; He, J.-Y.; Zhang, K.-S.; Liu, T.; Xu, W.; Huang, X.-J.; Kong, L.-T.; Liu, J.-H. Morphology-tunable WMoO nanowire catalysts for the extremely efficient elimination of tetracycline: Kinetics, mechanisms and intermediates. *Nanoscale* **2018**, *11*, 1047–1057. [[CrossRef](#)]
67. Xie, Z.J.; Feng, Y.P.; Wang, F.L.; Chen, D.N.; Zhang, Q.X.; Zeng, Y.Q.; Lv, W.Y.; Liu, G.G. Construction of carbon dots modified MoO₃/g-C₃N₄ Z-scheme photocatalyst with enhanced visible-light photocatalytic activity for the degradation of tetracycline. *Appl. Catal. B-Environ.* **2018**, *229*, 96–104. [[CrossRef](#)]
68. Li, J.Z.; Ma, Y.; Ye, Z.F.; Zhou, M.J.; Wang, H.Q.; Ma, C.C.; Wang, D.D.; Huo, P.W.; Yan, Y.S. Fast electron transfer and enhanced visible light photo-catalytic activity using multi-dimensional components of carbon quantum-dots@3D daisy-like In₂S₃/single-wall carbon nanotubes. *Appl. Catal. B-Environ.* **2017**, *204*, 224–238. [[CrossRef](#)]
69. Zhu, L.; Li, H.; Xia, P.; Liu, Z.; Xiong, D. Hierarchical ZnO Decorated with CeO₂ Nanoparticles as the Direct Z-Scheme Heterojunction for Enhanced Photocatalytic Activity. *ACS Appl. Mater. Interfaces* **2018**, *10*, 39679–39687. [[CrossRef](#)]
70. Guo, H.; Niu, C.G.; Zhang, L.; Wen, X.J.; Liang, C.; Zhang, X.G.; Guan, D.L.; Tang, N.; Zeng, G.M. Construction of direct Z-scheme AgI/Bi₂Sn₂O₇ nanojunction system with enhanced photocatalytic activity: Accelerated interfacial charge transfer induced efficient Cr(VI) reduction, tetracycline degradation and escherichia coli inactivation. *ACS Sustain. Chem. Eng.* **2018**, *6*, 8003–8018. [[CrossRef](#)]
71. Wang, L.; Zhu, B.; Cheng, B.; Zhang, J.; Zhang, L.; Yu, J. In-situ preparation of TiO₂/N-doped graphene hollow sphere photocatalyst with enhanced photocatalytic CO₂ reduction performance. *Chin. J. Catal.* **2021**, *42*, 1648–1658. [[CrossRef](#)]
72. He, R.; Liu, H.; Liu, H.; Xu, D.; Zhang, L. S-scheme photocatalyst Bi₂O₃/TiO₂ nanofiber with improved photocatalytic performance. *J. Mater. Sci. Technol.* **2020**, *52*, 145–151.
73. Wang, L.; Hong, Y.; Liu, E.; Wang, Z.; Chen, J.; Yang, S.; Wang, J.; Lin, X.; Shi, J. Rapid polymerization synthesizing high-crystalline g-C₃N₄ towards boosting solar photocatalytic H₂ generation. *Int. J. Hydrogen Energy* **2020**, *45*, 6425–6436. [[CrossRef](#)]
74. Dong, X.Y.; Huang, X.Q.; Wang, D.B.; Lei, Y.; Han, J.C.; Liang, X.F.; Wei, Q.L. Constructing crystalline needle-mushroom-like/ amorphous nanosheet carbon nitride homojunction by molten salt method for photocatalytic degradation of tetracycline hydrochloride. *J. Mater. Sci-Mater. El.* **2022**, *33*, 6043–6058. [[CrossRef](#)]
75. Zhang, P.; Wang, J.Q.; Gong, J.; Wang, K.; Li, Y.; Wu, X.Y. Fabrication of Ag/carbon nitride photocatalysts and their enhanced photocatalytic performance for tetracycline degradation. *Funct. Mater. Lett.* **2020**, *13*, 2051033. [[CrossRef](#)]
76. Chen, M.M.; Li, M.X.; Li, P.; Lee, S.L.J.; Tang, J.J.; Li, Q.; Lin, S.J. Enhanced visible light-driven photodegradation of tetracycline by salicylic acid-modified graphitic carbon nitride and toxicity assessment, *Environ. Sci. Pollut. R.* **2022**, *29*, 90768–90778. [[CrossRef](#)]
77. Wang, B.; Cao, Q.T.; Li, G.M.; Zhang, J. Preparation of non-polluting Tb-doped mesoporous carbon nitride photocatalyst and study on the efficacy and mechanism of degradation of antibiotics in water. *Environ. Sci. Pollut. R.* **2022**, *29*, 36337–36350. [[CrossRef](#)]
78. Wang, X.; Jing, H.X.; Gao, Y.L.; Xin, Y.Z.; Li, Q.L. CTAB assisted hydrothermal synthesis of 0D / 2D structure carbon quantum dots BiOIO₃ composite for photocatalytic degradation of tetracycline. *Inorg. Chem. Commun.* **2022**, *146*, 110209. [[CrossRef](#)]
79. Kuang, X.; Fu, M.; Kang, H.; Lu, P.; Bai, J.W.; Yang, Y.; Gao, S.X. A BiOIO₃/BiOBr n-n heterojunction was constructed to enhance the photocatalytic degradation of TC. *Opt. Mater.* **2023**, *138*, 113690. [[CrossRef](#)]

Disclaimer/Publisher's Note: The statements, opinions and data contained in all publications are solely those of the individual author(s) and contributor(s) and not of MDPI and/or the editor(s). MDPI and/or the editor(s) disclaim responsibility for any injury to people or property resulting from any ideas, methods, instructions or products referred to in the content.